ACS APPLIED MATERIALS & INTERFACES

Research Article

www.acsami.org

Aluminum Titania Nanoparticle Composites as Nonprecious Catalysts for Efficient Electrochemical Generation of H_2

Mohammed A. Amin,[*,†,‡] Emad M. Ahmed,[§,∥] Nasser Y. Mostafa,[†,⊥] Mona M. Alotibi,[§] Gitashree Darabdhara,[#,¶] Manash R. Das,[#,¶] Joanna Wysocka,[▽] Jacek Ryl,[▽] and Sayed S. Abd El-Rehim[‡]

[†]Materials Science and Engineering Group, Department of Chemistry, Faculty of Science, Taif University, 888 Hawiya, Taif, Saudi Arabia

[‡]Department of Chemistry, Faculty of Science, Ain Shams University, 11566 Abbassia, Cairo, Egypt

[§]Materials Science and Engineering Group, Physics Department, Faculty of Science, Taif University, 888 Hawiya, Taif, Saudi Arabia

[∥]Solid State Physics Department, National Research Center, Dokki, Giza 12311, Egypt

[⊥]Chemistry Department, Faculty of Science, Suez Canal University, Ismailia, Egypt

[#]Materials Sciences and Technology Division, CSIR-North East Institute of Science and Technology, Jorhat 785006, Assam, India

[¶]Academy of Scientific and Innovative Research, CSIR, Chennai 600113, India

[▽]Department of Electrochemistry, Corrosion and Materials Engineering, Chemical Faculty, Gdańsk University of Technology, Narutowicza Strasse 11/12, 80-233 Gdańsk. Poland

Supporting Information

ABSTRACT: In this paper, we demonstrated, for the first time, aluminum titania nanoparticle (Al-TiO_2 NP) composites with variable amounts of TiO_2 NPs as nonprecious active catalysts for the electrochemical generation of H_2. These materials were synthesized by mixing desired amounts of hydrogen titanate nanotubes (TNTs), fabricated here by a cost-effective approach at moderate hydrothermal conditions, with aluminum powder (purity 99.7%; size 35 μm). The mixture was compacted under an applied uniaxial stress of 300 MPa followed by sintering at 500 °C for 1 h. After sintering had been completed, all TNTs were found to convert to TiO_2 NPs (average particle size 15 nm). Finally, Al-$x$$TiO_2$ NP nanocomposites (x = 1, 3, 5, and 10) were obtained and characterized by scanning electron microscopy/energy-dispersive X-ray, X-ray diffraction, and X-ray photoelectron spectroscopy. The hydrogen evolution reaction (HER) activity of these materials was studied in 0.5 M H_2SO_4 at 298 K using polarization and impedance measurements. The nanocomposite of chemical composition Al-5% TiO_2 NPs showed the best catalytic performance for the HER, with an onset potential (E_{HER}), a Tafel slope (β_c), and an exchange current density (j_0) of −100 mV (RHE), 59.8 mV decade^{-1}, and 0.14 mA cm^{-2}, respectively. This HER activity is not far from that of the commercial platinum/carbon catalyst (E_{HER} = 0.0 mV, β_c = 31 mV dec^{-1}, and j_0 = 0.78 mA cm^{-2}). The best catalyst also exhibited good stability after 10000 repetitive cycles with negligible loss in current.

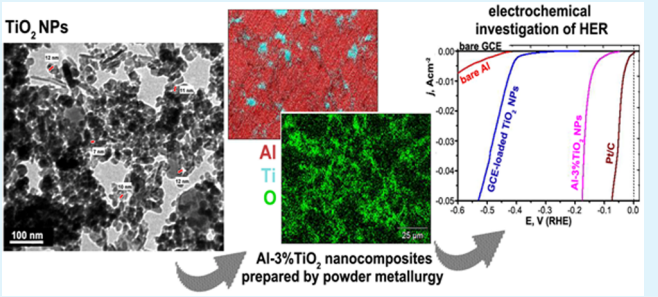

KEYWORDS: *nanocomposites, aluminum, titania nanoparticles, electrocatalysis, hydrogen evolution reaction*

1. INTRODUCTION

Rapid depletion in the fossil fuel reserves has paved the way toward increasing energy demand for new and environmentally friendly energy sources.[1] Since the beginning of the 1970s, molecular H_2 has been considered as a source of efficient, clean, and renewable energy capable of addressing global and environmental challenges.[2] Because H_2 does not exist in free form but is present in compounds like hydrocarbons and water, technologies toward the production of sustainable H_2 is thus crucial.[3] Another important aspect related with H_2 production is its storage and delivery to the users because it is highly explosive and flammable. Hence, H_2 production, storage, and transfer to its user is an important aspect of the hydrogen economy.[4]

Among different manners of H_2 production, like direct decomposition or partial oxidation of hydrocarbons,[5] water splitting reaction,[6] steam reforming of hydrocarbons,[7] etc., hydrolysis of metallic aluminum (Al) in an aqueous medium is noteworthy.[8] Most of the other methods are associated with their own disadvantages like high cost and less efficiency. Recently, H_2 generation via hydrolysis reaction of metal and

Received: May 14, 2016
Accepted: August 19, 2016

DOI: 10.1021/acsami.6b05630
ACS Appl. Mater. Interfaces XXXX, XXX, XXX−XXX

metal alloy has attracted wide importance because of the ease of H_2 storage, delivery, and low cost. Metallic Al having low cost, high abundance, and high activity readily reacts with water to produce around 3.7 wt % H_2, thus making it a highly favorable material for H_2 generation.

The production of H_2 via electrochemical water splitting reaction is another green and renewable technique. A platinum (Pt)-based electrocatalyst, because of its low reduction over potentials and fast proton reduction in acidic media, has been considered as the most effective catalyst toward the electrochemical generation of H_2. However, the high cost and scarcity of Pt makes the search for an alternative an important objective. A large number of Pt group metals such as Pt, ruthenium (Ru), rhodium (Rh), iridium (Ir), and palladium (Pd) are also considered as good alternative catalysts for the hydrogen evolution reaction (HER).[9] Other non-noble metals such as iron (Fe), cobalt (Co), nickel (Ni), and molybdenum (Mo) and their derivatives along with metal-free carbon-based materials are currently being investigated toward the HER catalytic reactions.[10−12] Other materials widely used toward the HER include supported metallic nanoparticles (NPs), like silver (Ag)[13] and gold (Au),[14] bimetallic alloy NPs such as Au−Pd,[15] Ni−Mo,[16] Co−Ni,[17] etc., core−shell NPs such as Ni@Pd/PEI-rGO,[18] NiAu@Au,[19] etc., transition-metal chalcogenides (MoS_2,[20] WS_2,[21] etc.), transition-metal carbides (WC NPs,[22] Mo_2C/graphene hybrid,[23] etc.), transition-metal nitrides (Mo nanosheets[24]), transition-metal borides (α-MoB micropar-ticle[25]), and transition-metal phosphides (CoP/Ti[26]).

TiO_2-based nanostructures have been developed for potential catalytic applications like in water splitting,[27] photocatalysis,[28] biomedical applications,[29] etc. Tubular TiO_2 structures are effectively used as electrodes without loss of conductivity at the titanium (Ti) and TiO_2 interface.[30] A large number of studies have focused on the doping of noble and non-noble metals like manganese (Mn), Ru, Pt, etc., to modify the high band gap of TiO_2 (3.0−3.2 eV) and simultaneously increase its electrochemical properties.[31,32]

The objective here, with a view of preparing a nonprecious stable and active catalyst, is to modify Al powders with different ratios of TiO_2 NPs. Such a modification is expected to reduce the electron−hole pair recombination of TiO_2, thus providing more reactive sites for electrocatalysis.[33] TiO_2 NPs were prepared in situ from hydrogen titanate nanotubes (TNTs) at 500 °C. In situ formation of TiO_2 NPs enabled us to obtain good dispersion of TiO_2 NPs as a filler. Moreover, Al, because of its advantages of natural abundance and high activity, is thought to help in generating more positive holes in the valence-band of TiO_2 which can increase the electrocatalytic activity of our synthesized Al-TiO_2 nanocomposites.[31,32]

Such nanocomposites were prepared here by mixing Al powder with increasing amounts of TNTs. The percent weight of TNTs was selected to give the percent weight of TiO_2, 1, 3, 5, and 10% based on 39% total weight loss of TNTs, as determined with thermogravimetric analysis/differential scanning calorimetry (TGA/DSC; Supporting Information, Figure S1). The mixed Al-TNT powders were hydrostatically compressed, followed by sintering at high temperature (500 °C), to form four disks with different chemical compositions, namely, Al-1% TiO_2, Al-3% TiO_2, Al-5% TiO_2, and Al-10% TiO_2. Literature revealed no reports on the use of a TiO_2 nanotube-doped Al powder to catalyze the HER. This makes it an entirely new study in which such low-cost and earth-abundant materials can be utilized toward the effective electrochemical generation of H_2.

2. EXPERIMENTAL SECTION

2.1. Materials. TNTs were prepared by adding 2.0 g of TiO_2 to 75 mL of a 10 M NaOH solution under vigorous magnetic stirring for about 1 h to form a white suspension. This suspension was then transferred into 100 mL Teflon-lined stainless steel autoclaves and allowed to react at 130 °C for 24 h to form sodium titanate nanotubes (STNTs). The produced STNT powder, after being cooled to room temperature, was washed several times with dilute HNO_3 (pH = 3) and then distilled water until neutralization. Finally, the washed powder was dried in air at 60 °C overnight to achieve the hydrogen TNTs. TNTs were calcined at 300 and 500 °C for 1 h.

The catalysts employed in this work were Al-TiO_2 NP nanocomposites of variable amounts of TiO_2 NPs that are supposed to be uniformly distributed within the Al matrix, to be tested as efficient electrocatalysts for the HER. These were prepared by powder metallurgy using Al powder (purity 99.7%; size 35 μm) and the above-synthesized TNTs. A mixture of Al powder and TNTs of a given composition was first mixed mechanically to get the required homogeneity. The nanocomposites were prepared in the form of a cylinder (2 cm length and 1 cm diameter) via compaction under an applied uniaxial stress of 300 MPa using 2 g of the mixed powder for each sample. After that, all cylinders were sintered at 500 °C for 1 h with a heating rate of 20 °C min^{-1}. At 500 °C, all TNTs were converted to TiO_2 NPs of an average particle size of 15 nm. Finally, nanocomposite materials of chemical compositions Al-x% TiO_2 NPs (x = 1, 3, 5, and 10) were obtained and were ready for electrochemical characterization.

2.2. Characterization. X-ray diffraction (XRD) analysis was carried out using an automated diffractometer (Philips PW1840), at a step size of 0.02°, a scanning rate of 2° in 2θ/min, and a 2θ range from 4° to 80°. After being coated with Au, the prepared catalysts' morphology was studied by means of a scanning electron microscope (JEOL model JSM-5600, Japan) equipped with a secondary electron detector (Hitachi model S-3400N, Japan) with an energy-dispersive X-ray (EDX) analyzer from ThermoFisher Scientific (U.K.), operating at a 20 kV accelerating voltage. The particle shape and size of the TNTs before and after sintering were studied by a transmission electron microscope (JEOL model JTEM-1230, Japan) operated at an accelerating voltage of 120 kV.

Chemical binding properties of the analyzed surface were investigated using X-ray photoelectron spectroscopy (XPS), with a Escalab 250Xi spectrometer (Thermofisher Scientific, U.K.), utilizing a monochromatic Al Kα source and charge neutralization by means of a flood gun. High-resolution spectra were recorded at a pass energy of 10 eV and an energy step size of 0.1 eV. Spectra were normalized, shifting the X axis versus peak of neutral C 1s (284.6 eV). Depth-profile analysis was provided by means of an ion gun, etching with Ar^+ ions (2000 V). Analysis software was provided by the manufacturer.

2.3. Electrochemical Measurements. Electrochemical studies were carried out in a standard three-electrode cell, with a saturated calomel electrode (SCE) as the reference electrode and a long spiral Pt wire as the counter electrode, connected to an Autolab PGSTAT30/FRA system (Ecochemie, The Netherlands). Measurements were conducted in a 200 mL deaerated aqueous solution of 0.5 M H_2SO_4; the solution was sparged for ∼30 min with Ar. The solution temperature was maintained at 25 ± 0.2 °C using a temperature-controlled water bath. Potentials were measured versus SCE and presented here against a reversible hydrogen electrode (RHE). More details concerning the conversion of SCE to RHE are presented in the Supporting Information, section II. The working electrode was then immediately immersed in the test solution.

The electrochemical techniques used to evaluate the electrochemical performances of catalysts toward the HER were linear potential sweep voltammetry (LSV) and electrochemical impedance spectroscopy (EIS). LSV measurements were carried out by sweeping the potential of the working electrode negatively at a scan rate of 5.0

DOI: 10.1021/acsami.6b05630
ACS Appl. Mater. Interfaces XXXX, XXX, XXX−XXX

mV s^{-1} starting from the corrosion potential (E_{corr}) up to a cathodic potential of −1.76 V vs RHE. Impedance measurements were carried out as a function of the applied cathodic overpotentials, namely, −0.06, −0.26, and −0.46 V vs RHE, using alternating-current signals of a peak-to-peak amplitude of 5 mV in the frequency range of 100 kHz to 10 mHz. HER Faradaic efficiencies for the studied catalysts were determined here by quantifying the amount of H_2 generated during controlled potential electrolysis by a gas chromatograph and dividing that by the amount of H_2 expected based on the charge passed (assuming 100% Faradaic efficiency) through the working electrode (WE) during that electrolysis. Measurements were conducted in a custom-made airtight electrolysis cell containing a 0.5 M H_2SO_4 solution by holding the electrode at −0.7 V vs RHE for 1 h. Gas chromatography was conducted on an Agilent 7890A gas chromatograph with a pneumatically operated automatic gas sampling valve to monitor the evolved H_2 gas. The electrolysis cell was connected to the gas chromatography system via bespoke airtight glass-to-metal adapters and copper tubing with an internal diameter of $^1/_8$ in. The oven temperature was set to 45 °C, and the carrier gas was Ar with a flow rate of approximately 3 mL min^{-1}.

The durability and stability of the best catalyst was evaluated, as described elsewhere,[14] by 24 h of chronoamperometry measurements at a fixed cathodic overpotential and continuous potential cycling up to 10000 cycles. Each run was repeated at least three times to ensure the reproducibility of the results. The reported data are found to be statistically significant; their arithmetic mean and standard deviation were calculated and reported.

3. RESULTS AND DISCUSSION

3.1. Structure Properties of the Prepared TNTs. XRD patterns of TNTs annealed at different temperatures are shown in Figure 1. The sample annealed at 100 °C shows a typical diffraction of layered titanates. The interlayer space gives a strong broad peak at around $2\theta = 10°$. According to ref 34, the composition of the TNT sample is very close to that of $H_2Ti_3O_7$ (hydrogen titanate with a layered structure).

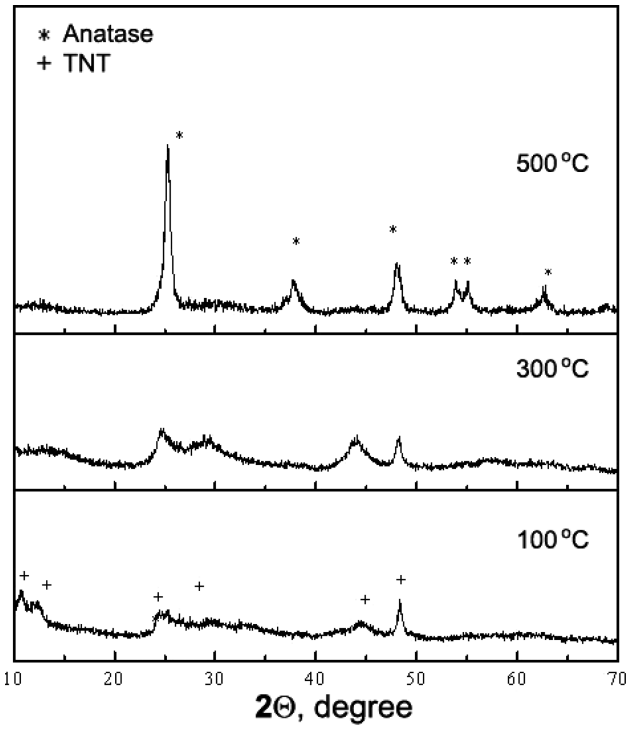

Figure 1. XRD patterns recorded for hydrogen TNTs thermally treated at 100, 300, and 500 °C for 1 h.

However, for the sample treated at 300 °C, the XRD peak at $2\theta = 10°$ disappears, indicating the collapse of the layer structure, and all of the other peaks of hydrogen titanates are still observed. At 500 °C, all nanotubes are converted to anatase (TiO_2). Figure 2 shows transmission electron microscopy (TEM) micrographs of the TNTs calcined at 300 and 500 °C. Figure 2a indicates that the tubular structure of TNTs is still maintained up to 300 °C. However, at 500 °C, all TNTs tubular structures are converted to TiO_2 NPs (9−16 nm).

3.2. Structure Properties of the Prepared Nanocomposites. Figure 3 shows the XRD patterns of the prepared Al-x% TiO_2 NP (x = 1, 3, 5, and 10) nanocomposites. The observed peaks are assigned to the α-Al and TiO_2 phases. The main XRD peak of TiO_2 is located at 25.379° diffracted from the (101) plane. The intensity of this diffraction peak is enhanced, as expected, with an increase in x. The lattice parameter, crystallite size, and microstrain of α-Al calculated from the (111), (200), (220), (311), and (222) XRD lines are presented in the Supporting Information, Table S1. It is seen that the lattice parameter of the α-Al phase increases with x, referring to expansion of the Al (atomic radius equal to 143 Å) unit cell. This expansion in the Al unit cell is most probably attributed to the incorporation of Ti atoms with a larger atomic radius (170 Å) as a result of dissolution of Ti in the α-Al phase. Moreover, for the composite of chemical composition Al-10% TiO_2 (where the XRD peaks due to TiO_2 are considerable enough to deal with), the average crystallite size and lattice strain of TiO_2 calculated from (101), (200), (105), (211), and (204) XRD lines are 35 nm and 0.304, respectively. This means that the average crystallite size of the TiO_2 particles included in our synthesized nanocomposite materials is in the nanometer scale, even after sintering.

Scanning electron microscopy (SEM) micrographs and EDX spectroscopy (Supporting Information, Figure S2) of as-prepared Al-x% TiO_2 NP composites were performed as a function of the content of the TiO_2 NPs included in the matrix, x = 1, 3, 5, and 10. The EDX spectra of these materials prove the existence of Ti and O; their ratios increase with an increase in the content of TiO_2 NPs. It is shown that the morphology of these nanocomposites gets more porous with an increase in the content of TiO_2 NPs. All synthesized Al-TiO_2 NP composites exhibit almost homogeneous composition except the composite with the highest content of TiO_2 NPs (Al-10% TiO_2 NPs; Supporting Information, Figure S2, image d). EDX chemical analysis for Al, Ti, and O was presented in detail in Figure 4. TiO_2 NPs are well distributed through the Al matrix for Al-1% TiO_2, Al-3% TiO_2, and Al-5% TiO_2; however, in the last case, the chemical composition on the surface is less homogeneous because TiO_2 NPs start to accumulate as larger structures. The size of the agglomerations does not exceed 20 μm. On the contrary, the NPs of TiO_2 are not well distributed through the matrix of the Al-10% TiO_2 NP composite but accumulated in isolated regions, leading to the observed nonhomogeneous composition. The inhomogeneous distribution of TiO_2 NPs through the matrix of the Al-10% TiO_2 NPs composite is quite evident from the EDX element mapping study, shown in Figure 5.

High-resolution XPS spectra were recorded in the Al 2p, O 1s, and Ti 2p energy ranges. The goal of the analysis was to confirm the homogeneous incorporation of TiO_2 NPs into Al. The results are presented in Figure 6. The incorporation of TiO_2 NPs on the Al surface was confirmed on the basis of registered spectra. The region attributed to titania was

DOI: 10.1021/acsami.6b05630
ACS Appl. Mater. Interfaces XXXX, XXX, XXX−XXX

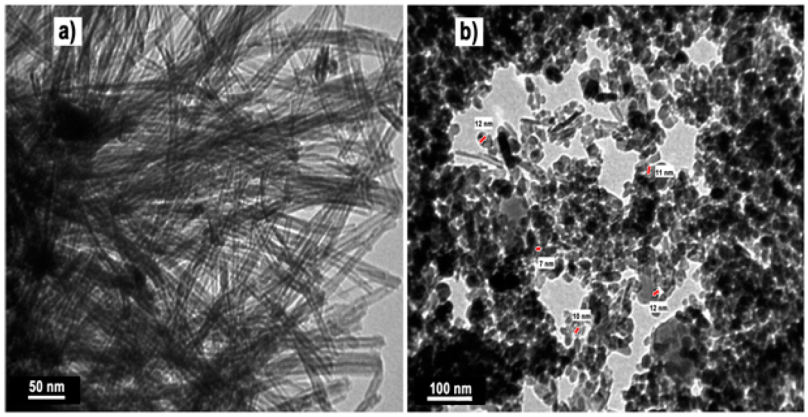

Figure 2. TEM micrographs of prepared TNTs after calcination at (a) 300 and (b) 500 °C.

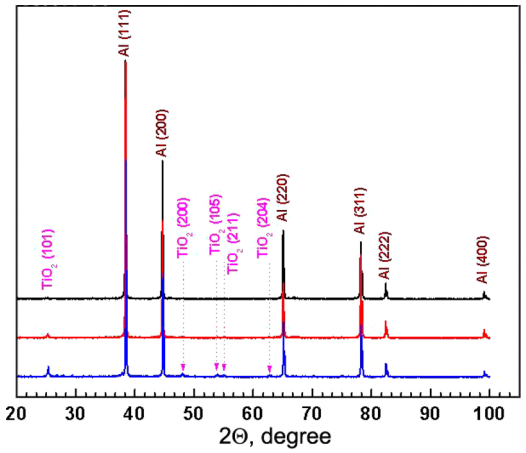

Figure 3. XRD patterns of Al-x% TiO_2 NP nanoconposites, where x = 1, 5, and 10.

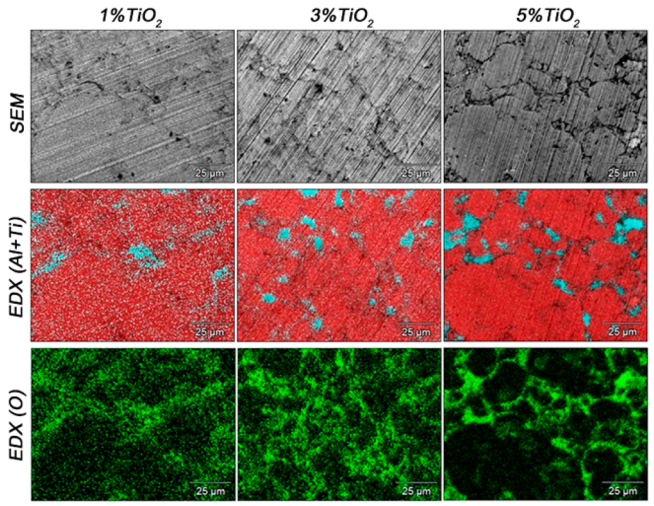

Figure 4. SEM micrographs and corresponding EDX chemical maps acquired for Al with 1%, 3%, and 5% TiO_2 NPs incorporated: Al (red); Ti (light blue); O (green). Magnification 1000×.

characterized with a single peak doublet: Ti $2p_{1/2}$ and Ti $2p_{3/2}$. The position of Ti $2p_{3/2}$ is 459.3 eV and corresponds to TiO_2 according to numerous reports.[35,36] Three peak doublets can be distinguished for Al 2p spectra and were used for deconvolution purposes. One is characteristic for metallic Al (Al_m), with the Al $2p_{3/2}$ peak located at 73.4 eV and the remaining two (Al_{ox1} and Al_{ox2}) corresponding to oxidized metal. Al_{ox1} is in energy range typical for aluminum oxide (Al_2O_3; 76.1 eV), while Al_{ox2} most likely represents $Al(OH)_3$ and/or AlOOH (74.6 eV). These results are in good agreement with other studies.[37−39] The higher incorporation of Ti also resulted in a slight shift of the Al_m peak into more negative binding energy values. This shift does not exceed 0.3 eV for the 5% TiO_2 NP sample and is in good agreement with the results obtained for Ti−Al alloys. In their study, Diplas et al. observed that the addition of Ti as an alloying component of Al results in a similar behavior.[40] The total shares of each deconvoluted peak in the high-resolution XPS spectra are summarized in Table S2 (Supporting Information).

These results confirm that the amount of incorporated TiO_2 NPs is proportional to the share of Ti in the investigated spectra. The pure Al sample had the lowest share of O_2 and the highest share of the Al_m subpeak; therefore, a conclusion was drawn that the incorporation of TiO_2 NPs slightly increases the thickness of the passive layer. A depth-profile analysis was then performed to determine the homogeneity of this layer. Figure 7 shows, as a representative example, the depth-profile analysis obtained for the Al-5% TiO_2 NP sample. Similar results were obtained for 1 and 3% TiO_2 NPs (Supporting Information, Figure S3). Ion-beam etching revealed a slow diminishing of the Al_{ox2} and O_{ox2} subpeaks with the depth of the oxide layer, proving a higher level of hydration of the outer film. In a similar way, C contamination originating from the exposure of samples to air conditions is also only prominent in the outer film and diminishes with the depth. This contamination affects O_{ox2} the most. On the other hand, the signal from TiO_2 remains constant with in-depth analysis, proving its good homogeneity. After 7000 s of etching, the layer was removed, fully revealing the Al_m and TiO_2 substructures.

3.3. Electrochemical Generation of H_2 Gas.

3.3.1. Cathodic Behavior of Al-TiO_2 Nanocomposites in Sulfuric Acid Solutions. A literature survey revealed no reports concerning the electrochemical activity of Al-TiO_2 nanocomposites toward the HER. This was the reason why the HER activity of our synthesized Al-TiO_2 NP composites was evaluated here. The electrochemical performances of both bare sintered Al and Pt/C electrocatalysts were also investigated for comparison. To assess the impact (catalytic influence) of TiO_2 NPs themselves on the kinetics of the HER, the HER polarization curves of TiO_2 NPs alone were also constructed. In this respect, the NPs of TiO_2 were loaded on glassy carbon electrodes (GCEs) with different densities (0.0016, 0.0046,

DOI: 10.1021/acsami.6b05630
ACS Appl. Mater. Interfaces XXXX, XXX, XXX−XXX

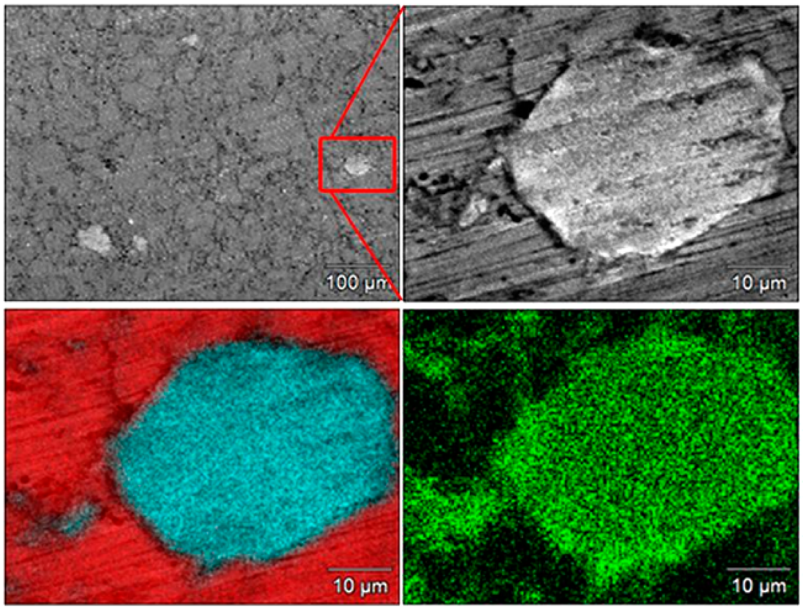

Figure 5. SEM/EDX of Al-10% TiO_2 NPs revealing a heterogeneous TiO_2 distribution and its local accumulation. EDX chemical maps: Al (red); Ti (light blue); O (green). Magnification 200× (top left) and 2000× (other images).

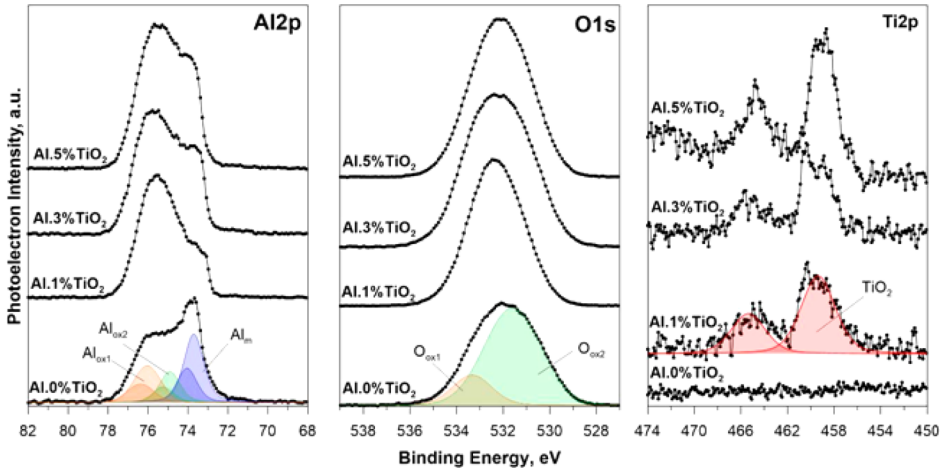

Figure 6. High-resolution XPS spectra recorded for Al $2p_3$, O 1s, and Ti $2p_3$, acquired for Al with 1%, 3%, and 5% TiO_2 NPs incorporated, including subpeaks used for deconvolution.

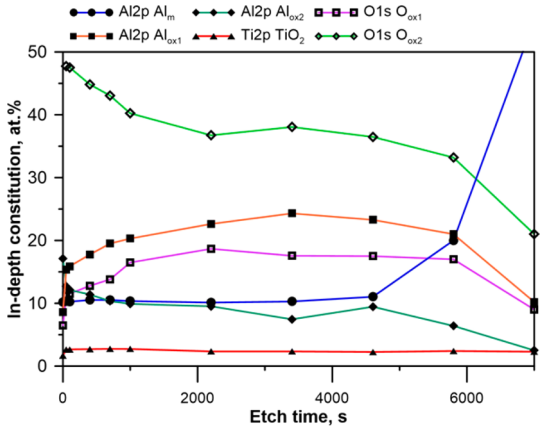

Figure 7. Depth-profile analysis for the Al-5% TiO_2 NP sample on the basis of high-resolution XPS spectra. Ion energy = 2000 V.

0.0075, and 0.018 g cm^{-2}), and their HER catalytic performances were then measured in a comparison with the bare GCE. Figure 8a collects the recorded HER polarization curves. Measurements were carried out in 0.5 M H_2SO_4 solutions at a scan rate of 5.0 mV s^{-1} at 25 °C.

It is seen that the Pt/C electrode (curve 11) shows the lowest onset for the HER (E_{HER} ∼ 0.0 mV) and highest cathodic currents, indicating its superior HER electrocatalytic activity.[41] By contrast, bare sintered Al (curve 1) exhibited little HER activity with a larger E_{HER} of about −520 mV and much lower catalytic currents. The bare GCE (curve 2) exhibits a minimal background activity for the HER. The cathodic polarization curves of GCE-loaded TiO_2 NP electrodes (curves 3−6) showed, compared with that of bare GCE (curve 2), increased HER catalytic activity. These results reflect the catalytic activity of the loaded TiO_2 NPs toward the HER. Such HER activity of TiO_2 NPs is found to be enhanced with a loading density of up to 0.0075 g cm^{-2}, curve 7. A further increase in the loading density of TiO_2 NPs from 0.0075 g cm^{-2}

DOI: 10.1021/acsami.6b05630
ACS Appl. Mater. Interfaces XXXX, XXX, XXX−XXX

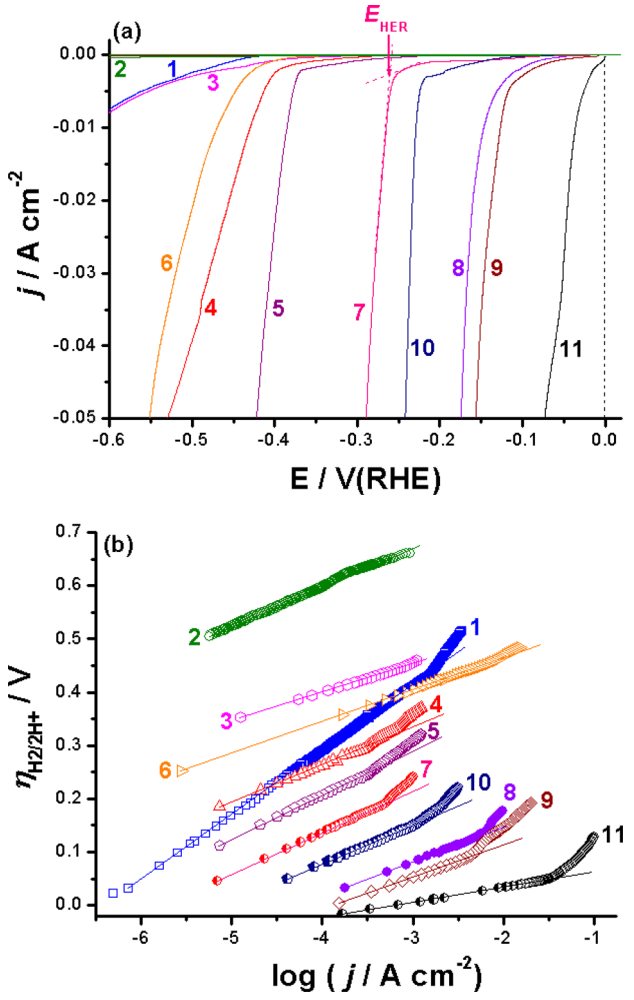

Figure 8. Electrocatalytic hydrogen evolution of different catalysts: (a) polarization curves for the HER on (1) bare sintered Al; (2) bare GCE; (3) GCE-loaded TiO_2 NPs (loading density 0.0016 g cm^{-2}); (4) GCE-loaded TiO_2 NPs (loading density 0.0046 g cm^{-2}); (5) GCE-loaded TiO_2 NPs (loading density 0.0075 g cm^{-2}); (6) GCE-loaded TiO_2 NPs (loading density 0.018 g cm^{-2}); (7) Al-1% TiO_2 NPs; (8) Al-3% TiO_2 NPs; (9) Al-5% TiO_2 NPs; (10) Al-10% TiO_2 NPs; (11) a commercial Pt/C catalyst. Measurements were carried out in 0.5 M H_2SO_4 solutions at a scan rate of 5 mV s^{-1} at 25 °C. (b) Tafel plots for the tested catalysts derived from part a.

(curve 5) to 0.018 g cm^{-2} (curve 6) has resulted in an obvious decrease in the catalytic activity. These findings can be explained on the basis that an increased loading density of the NPs of TiO_2 increases their population. This, in turn, might increase TiO_2 NP aggregation, which acts against the electrocatalytic activity.[42]

The overpotentials of the Al-TiO_2 composite catalysts (curves 7−10) are smaller, with higher cathodic currents, than those recorded for TiO_2 NPs alone (curves 3−6) and bare sintered Al (curve 1). These findings reveal that the HER proceeds faster when sintered Al and TiO_2 NPs are brought together as composite materials than if they are working individually. On the basis of these results, it can be proposed here that the Al-TiO_2 NP composite catalysts show high HER electrocatalytic properties via cooperative interactions (synergistic effects) between Al and TiO_2 NPs.

A comparison among curves 7−10 reveals that the HER activity of the synthesized catalysts increased with an increase in the amounts of TiO_2 NPs in the composite. This is quite clear from the shift of E_{HER} toward more active potential values with increasing TiO_2 NP content. This active shift of E_{HER} gives rise to higher exchange current densities and larger cathodic currents at low overpotentials (see later), indicating increased kinetics for the HER. In other words, the higher the amount of TiO_2 NPs added to the Al matrix, the higher the number of TiO_2 NPs included in a given area of the matrix. Thus, population of the active catalytic sites (the electrocatalytic activity of TiO_2 NPs toward the HER is confirmed from the polarization measurements of the GCE-loaded TiO_2 NP cathodes; Figure 8a, curves 3−6) available for the HER increased, favoring H_2 generation at lower overpotentials.[14] This increase in the HER activity has occurred systematically when the amount of added TiO_2 NPs increased from 1.0 wt % (curve 7) up to 5.0 wt % (curve 9).

However, a further increase in the amount of added TiO_2 NPs, i.e., beyond 5.0 wt % (curve 10), exerted a marked negative influence on the catalytic activity of the tested materials. This negative impact of TiO_2 NPs on the HER activity of catalyst Al-10% TiO_2 NPs can be attributed to the inhomogeneous distribution of TiO_2 NPs in the matrix, as evidenced from EDX element mapping (Figure 5). This inhomogeneous distribution of TiO_2 NPs may originate from the higher content of TiO_2 NPs (10%) included in the matrix of that catalyst, which permits aggregations most likely due to coalescence and agglomeration processes.[13,14] On the basis of these results, the HER catalytic performances of the tested nanocomposite catalysts are ranked as Al < Al-1% TiO_2 NPs < Al-10% TiO_2 NPs < Al-3% TiO_2 NPs < Al-5% TiO_2 NPs.

3.3.1.1. Analysis of the Polarization Curves (Tafel Plots) and Origin of the Catalytic Activity. Figure 8b depicts the Tafel plots for all tested materials derived from the corresponding LSV data shown in Figure 8a. To extract the important kinetic parameters characterizing the kinetics of the HER (Table 1), the linear portions of these plots were fitted to the Tafel equation for a cathodic reaction, expressed as[43]

$$\eta = (2.3RT/n\alpha F)\log j_0 - (2.3RT/n\alpha F)\log j \quad (1)$$

where η is the cathodic overpotential and j_0 is the exchange current density (the current density here is referred to as the working electrode's geometric area), n is the number of electrons involved in the electrode reaction, and α is the charge-transfer coefficient. Obviously, the parameters vary according to the type and chemical composition of the tested materials. The values of j_0, calculated via Tafel extrapolation until zero overpotential η_0 (Supporting Information, Figure S4), recorded for the studied GCE-loaded TiO_2 NPs are much higher than that recorded for the bare GCE, demonstrating the catalytic influence of TiO_2 NPs on the HER. For instance, the GCE-loaded TiO_2 NPs with a loading density of 0.0075 g cm^{-2} recorded the highest j_0 value (3.16×10^{-4} mA cm^{-2}) among the other tested GCE-loaded TiO_2 NPs (2.5×10^{-8}, 1.58×10^{-5}, and 1.38×10^{-7} mA cm^{-2} for loading densities of 0.0016, 0.0046, and 0.018 g cm^{-2}, respectively), which is 4.3×10^5 times greater than that measured for the bare GCE (7.4×10^{-10} mA cm^{-2}). Further inspection of Table 1 reveals that the parameters of the HER are significantly affected by treating Al with TiO_2 NPs to different extents depending on the amount of TiO_2 NPs included in the Al matrix. For instance, a Al-5% TiO_2 NP composite catalyst (the best catalyst here) exhibited the highest j_0 value (0.14 mA cm^{-2}) among the other studied composite catalysts (1.8×10^{-3}, 5.6×10^{-2}, and 8.0×10^{-3} mA

DOI: 10.1021/acsami.6b05630
ACS Appl. Mater. Interfaces XXXX, XXX, XXX−XXX

Table 1. Mean Value (Standard Deviation) of the Electrochemical Kinetic Parameters for the HER on the Surfaces of Our Synthesized Al-x% TiO_2 (x = 1, 3, 5, and 10) Nanocomposites in a 0.5 M H_2SO_4 Solution at 25 °C, in a Comparison with Those Recorded for Bare Al (as Sintered), TiO_2 NPs Alone (with Different Loading Densities on a GCE[a]), and Pt/C

tested cathode	onset potential (E_{HER}, mV vs RHE)	Tafel slope (mV dec^{-1})	exchange current density (j_0, mA cm^{-2})	overpotential at j = 10 mA cm^{-2} (η_{10}, mV)
bare Al	−520(9)	124(2.4)	4.4(0.05) × 10^{-4}	535(6)
bare GCE	−636(11.6)	75(1.2)	7.4(0.07) × 10^{-10}	742(9.2)
GCE-loaded TiO_2 NPs (loading density 0.0016 g cm^{-2})	−550(12)	52(1.4)	2.5(0.06) × 10^{-8}	502(5.6)
GCE-loaded TiO_2 NPs (loading density 0.0046 g cm^{-2})	−481(8)	69(1.5)	1.58(0.03) × 10^{-5}	397(4.2)
GCE-loaded TiO_2 NPs (loading density 0.0075 g cm^{-2})	−374(5)	85(1.4)	3.16(0.05) × 10^{-4}	373(4.8)
GCE-loaded TiO_2 NPs (loading density 0.018 g cm^{-2})	−434(6)	59(1.2)	1.38(0.03) × 10^{-7}	463(5.4)
Al-1% TiO_2 NPs	−259(4)	78(1.06)	1.8(0.04) × 10^{-3}	292(3)
Al-3% TiO_2 NPs	−150(3)	62(1.06)	5.6(0.04) × 10^{-2}	145(4)
Al-5% TiO_2 NPs (the best catalyst)	−110(3)	59.8(1.03)	0.14(0.005)	112(3)
Al-10% TiO_2 NPs	−224(5)	72(1.1)	8(0.12) × 10^{-3}	220(5)
Pt/C	∼0.0(0.05)	31(0.2)	0.78(0.012)	∼2(0.035)

[a]Glassy carbon electrode.

cm^{-2} for Al-1% TiO_2 NP, Al-3% TiO_2 NP, and Al-10% TiO_2 NP composite catalysts, respectively), which is ∼3.2 × 10^2 times greater than that recorded for the bare sintered Al electrode (4.4 × 10^{-4} mA cm^{-2}) and 4.4 × 10^2 times greater than the best GCE-loaded TiO_2 NPs (3.16 × 10^{-4} mA cm^{-2}), the one with a loading density of 0.0075 g cm^{-2}. These results demonstrate that the Al-TiO_2 NP composite catalysts possess much higher catalytic activity toward the HER than the bare sintered Al and TiO_2 NPs alone. However, the Pt/C electrocatalyst recorded a j_0 value of 0.78 mA cm^{-2}, which is ∼6.0 times greater than that measured for the Al-5% TiO_2 NP composite catalyst. That means that the HER electrocatalytic activity of our best catalyst (Al-5% TiO_2 NPs) is still relatively low compared with that of Pt/C and needs further improvement. However, its current HER activity was found to be comparable with those of some other newly reported highly efficient nonprecious electrocatalysts (Supporting Information, Table S4).

The overpotential at a given current density is another important parameter characterizing the apparent electrode activity.[44−46] The values of the overpotential at a current density of 10 mA cm^{-2} (η_{10}) recorded for the tested catalysts (Table 1) decrease markedly, thus favoring H_2 generation with high cathodic currents at lower overpotentials, in comparison with that of the bare Al electrode (535 mV). Here again, an Al-5% TiO_2 NP composite catalyst recorded the lowest η_{10} (112 mV) among the studied composite catalysts (292, 145, and 220 mV for Al-1% TiO_2 NP, Al-3% TiO_2 NP, and Al-10% TiO_2 NP catalysts, respectively). The same trend was observed considering the values of E_{HER}; the lowest value of E_{HER} (−110 mV) is measured for an Al-5% TiO_2 NP catalyst. These findings add other evidence that the treatment of Al with TiO_2 NPs significantly enhances its HER activity, with the Al-5% TiO_2 NP catalyst being the most effective one.

The HER inherent activity of our synthesized nanocomposites was also evaluated by their measured β_c values (Table 1), which showed a marked decrease from 124 mV dec^{-1} for bare Al to about 60 mV dec^{-1} for the two best catalysts, namely, Al-3% TiO_2 and Al-5% TiO_2 NPs. This decrease in the β_c values indicates accelerated kinetics of the HER upon treatment of Al with TiO_2 NPs because lower Tafel slopes suggest an increased number of accessible catalytic active sites.[47,48] In acidic media, the HER proceeds via three possible reaction steps.[47−49] These include the following: (i) a primary discharge step (Volmer reaction, eq 2), followed by either (ii) an electrochemical desorption step (Heyrosky reaction, eq 3) or (iii) a recombination step (Tafel reaction, eq 4).

$$H_3O^+ + e^- = H_{ads} + H_2O, \text{ with } \beta_c = 2.3RT/\alpha F \sim 120 \text{ mV} \quad (2)$$

$$H_{ads} + H_3O^+ + e^- = H_2 + H_2O, \text{ with } \beta_c = 2.3RT/(1+\alpha)^F \sim 40 \text{ mV} \quad (3)$$

$$H_{ads} + H_{ads} = H_2, \text{ with } \beta_c = 2.3RT/2F \sim 30 \text{ mV} \quad (4)$$

where R is the ideal gas constant, T is the temperature, α is the symmetry coefficient, and F is the Faraday constant. Indeed, it is difficult here to establish the HER mechanism over our catalysts because their measured β_c values (78, 62, 59.8, and 72 mV dec^{-1} for Al-1% TiO_2 NPs, Al-3% TiO_2 NPs, Al-5% TiO_2 NPs, and Al-10% TiO_2 NP catalysts, respectively) are not close to the three standard values for the HER reaction steps shown in eqs 2−4. However, the Tafel slope of ∼60 mV dec^{-1} recorded for the two best catalysts may suggest that the HER proceeds on their surfaces via both Volmer and Volmer−Heyrovsky mechanisms (eqs 2 and 3, respectively). On the other hand, the large Tafel slope measured for bare Al (124 mV dec^{-1}) may refer to the Volmer reaction (eq 2) as the mechanism responsible for the HER over a bare Al surface.

The HER activity per site of a catalyst is evaluated by what is called the turnover frequency (TOF), the number of H_2 molecules produced per second per active site.[50,51] TOF values were calculated here at 250 mV overpotential using the S_{BET} values measured for the tested catalysts (the procedure is reported in the Supporting Information, and the obtained TOF values are collected in Table S3). It is shown that the TOF of Al significantly enhanced upon mixing with TiO_2 NPs. Even low concentrations of TiO_2 NPs had a remarkable increase in the TOF. For instance, the TOF value of the Al-1% TiO_2 NP

DOI: 10.1021/acsami.6b05630
ACS Appl. Mater. Interfaces XXXX, XXX, XXX−XXX

catalyst (5.4×10^{-2} H_2/s per active site) is about 14 times greater than that measured for bare Al (3.95×10^{-3} H_2/s per active site). These results confirm that the combination of Al and TiO_2 NPs greatly enhances the HER kinetics over the Al-TiO_2 NP composite catalysts. Here again, Al-5% TiO_2 NPs catalyst recorded the highest TOF value (1.6 H_2/s per active site), which is more than 400 times higher than that of bare Al (3.95×10^{-3} H_2/s per active site), among the other tested Al-TiO_2 NP composite catalysts (5.4×10^{-3}, 1.37, and 0.32 H_2/s per active site for Al-1% TiO_2, Al-3% TiO_2, and Al-10% TiO_2 NPs, respectively).

The Faradaic efficiency (ε) of the HER was also determined for the studied catalysts to further evaluate their electrocatalytic activity. The value of ε was determined by measuring the amount of H_2 produced per hour using gas chromatography during electrolysis (a potentiostatic experiment where the tested catalyst was held at −0.7 V vs RHE for 1 h in a 0.5 M H_2SO_4 solution) and dividing that by the amount of H_2 expected (calculated) based on the charge passed (assuming 100% Faradaic efficiency) during that electrolysis. Figure 9 is a representative example for the amounts of H_2 (calculated and measured, expressed as millimoles) for the best catalyst (Al-5% TiO_2 NPs) during 1 h of this electrolysis process. H_2 versus time of electrolysis plots for the rest of the catalysts and Pt/C are shown in Figure S5 (Supporting Information). Charge versus time plots recorded for our synthesized Al-TiO_2 NP catalysts, in a comparison with Pt/C, during 1 h of controlled potential electrolysis are also presented in the Supporting Information, Figure S6. The obtained data are presented here in Table 4. Once again, the nanocomposite of chemical composition Al-5% TiO_2 NPs presented itself as the best catalyst for the HER in this work. It yielded the highest amount of H_2 (11.87 μmol h^{-1}), as measured by gas chromatography, among the other tested catalysts (6.24, 8.82, and 7.28 μmol h^{-1} for Al-1% TiO_2, Al-3% TiO_2, and Al-10% TiO_2, respectively) with a Faradaic efficiency of ∼93% (not far from that of Pt, ∼100%).

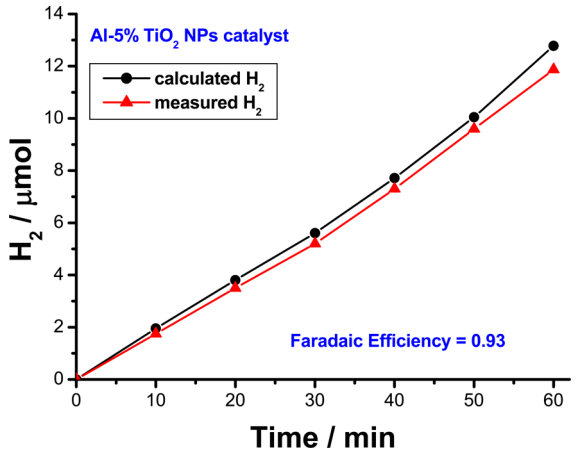

Figure 9. Generated H_2 calculated from the amount of charge passed (assuming 100% Faradaic efficiency) and measured from gas chromatography during 1 h of controlled potential electrolysis of the best catalyst (Al-5% TiO_2 NPs) at −0.7 V vs RHE in a 0.5 M H_2SO_4 aqueous solution.

3.3.1.2. Impedance Studies. To further clarify the role of TiO_2 NPs in enhancing the kinetics of the HER on the surfaces of our nanocomposite materials, EIS measurements were carried out at −0.26 V vs RHE cathodic potential, employing a wide frequency range (10000 Hz to 10 mHz; Figure 10). The impedance responses of Pt/C, bare Al, bare GCE, and GCE-loaded TiO_2 NPs were also included for comparison. Different features of these impedance plots deserve comments. The complex-plane impedance plots of Pt/C (curve 11), bare GCE (curve 2) and GCE-loaded TiO_2 NPs (curves 3−6) exhibit a single capacitive loop. A one-time constant process is also displayed on the corresponding Bode plots (Supporting Information, Figure S7). This capacitive loop can be assigned to the charge-transfer process of H^+ reduction at the electrocatalyst/electrolyte interface, which is a combination of charge-transfer resistance (R_{ct}) and the corresponding capacitance (C_{dl}).[52]

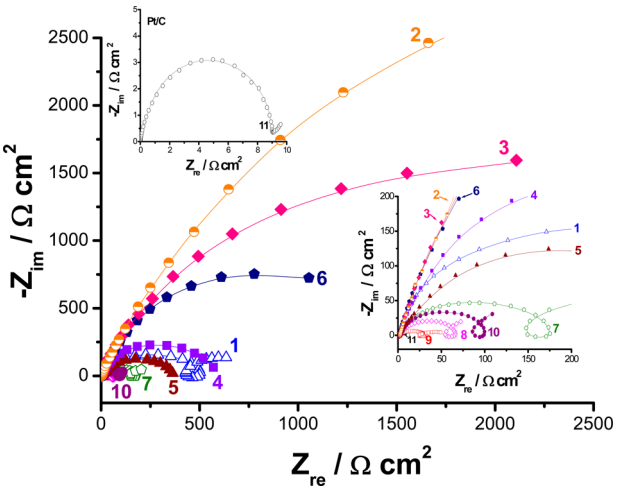

Figure 10. Complex-plane impedance plots recorded for the tested materials: (1) bare sintered Al; (2) bare GCE; (3) GCE-loaded TiO_2 NPs (loading density 0.0016 g cm^{-2}); (4) GCE-loaded TiO_2 NPs (loading density 0.0046 g cm^{-2}); (5) GCE-loaded TiO_2 NPs (loading density 0.0075 g cm^{-2}); (6) GCE-loaded TiO_2 NPs (loading density 0.018 g cm^{-2}); (7) Al-1% TiO_2 NPs; (8) Al-3% TiO_2 NPs; (9) Al-5% TiO_2 NPs, ;(10) Al-10% TiO_2 NPs; (11) a commercial Pt/C catalyst. Measurements were carried out in 0.5 M H_2SO_4 solutions at a cathodic potential of −0.26 V vs RHE at 25 °C.

On the other hand, the Nyquist plots of bare Al (curve 1) and Al-TiO_2 nanocomposite catalysts (curves 7−10) showed three times the constant processes. These are two depressed capacitive loops at high- and low-frequency values separated by an inductive loop at intermediate frequencies. Similar impedance responses were previously obtained.[53−55] The first time constant can be assigned to the combination of charge-transfer resistance and double-layer capacitance.[54,55] The inductive loop may be attributed to the relaxation process obtained by adsorption species like H^+_{ads}[54,55] (eq 2). With a further decrease of the frequency, H_2 may form either by an electrochemical desorption step (Heyrosky reaction, eq 3) or via a recombination step (Tafel reaction, eq 4), forming the second capacitive loop observed at the low-frequency values. It is observed that, as the applied cathodic potential is made more negative, the diameters of the semicircles observed in Figure 10 decrease for all of the studied materials (Supporting Information, Figure S8). These findings indicate that all semicircles, and hence the total impedance, are associated with the HER kinetics.

DOI: 10.1021/acsami.6b05630
ACS Appl. Mater. Interfaces XXXX, XXX, XXX−XXX

Table 2. Mean Value (Standard Deviation) of the Various Electrochemical Parameters Obtained from Impedance Measurements for the HER on the Surfaces of GCE-Loaded TiO_2 NPs (with Different Loading Densities) and Pt/C[a]

tested cathode	R_s (Ω cm^2)	Q [s^n(ω^{-1} cm^{-2})]	R_{ct} (Ω cm^2)	n	C (μF cm^{-2})
bare GCE	2.2(0.05)	8.85(0.18)	10537(32)	0.92	7.2(0.12)
GCE-loaded TiO_2 NPs (loading density 0.0016 g cm^{-2})	2.05(0.04)	26.29(0.3)	4210.9(21)	0.87	18.92(0.26)
GCE-loaded TiO_2 NPs (loading density 0.0046 g cm^{-2})	2.02(0.08)	48.27(0.66)	545.3(6.7)	0.86	26.7(0.31)
GCE-loaded TiO_2 NPs (loading density 0.0075 g cm^{-2})	2.35(0.06)	79.65(0.96)	365.53(5.2)	0.83	38.6(0.42)
GCE-loaded TiO_2 NPs (loading density 0.018 g cm^{-2})	2.12(0.04)	32.03(0.4)	1551(17.92)	0.86	19.65(0.22)
Pt/C	1.98(0.02)	1661.7(1.31)	9.1(0.15)	0.96	1395.4(2.11)

[a]Measurements were performed in 0.5 M H_2SO_4 solutions at a cathodic potential of −0.5 V (SCE) at 25 °C.

It is obvious from the impedance plots that our catalysts, namely, Al-(1−10%) TiO_2 NPs, exhibited a significantly lower impedance, which depends on % TiO_2, than that of bare Al, confirming their high HER activity. This significantly reduced impedance refers to fast HER kinetics over the surfaces of our synthesized catalysts. The NPs of TiO_2 included in the Al matrix act as catalytic adsorption sites that promote electron transfer during the H^+ reduction process. This, in turn, leads to a semicircle with reduced diameter, and hence diminished charge-transfer resistance results. However, in order to gain more insight on the kinetics of the HER, extracting the various electrochemical kinetic parameters associated with the HER, the measured impedance data were simulated using nonlinear-least-squares (NLS) fitting analysis software. The electrical circuit models used to study the kinetics of the HER are depicted in Figure S9 (Supporting Information) and fully described elsewhere.[54]

Analysis of the impedance plots revealed that the slopes of the log |Z| against log f plots (Supporting Information, Figure S7) are not −1, and the center of all capacitive loops lies below the real axis. These findings refer to the depressed nature of the semicircles, most probably because of the porous morphology of the tested materials (revisit Supporting Information, Figure S2). Thus, a constant-phase element (CPE), the impedance of which is given by eq 5,[56,57] was used to describe this behavior properly.

$$Z_{CPE} = Q^{-1}(j\omega)^{-n} \quad (5)$$

where Q is the CPE constant (a proportional factor), ω is the angular frequency (in rad s^{-1}), $j^2 = -1$ is the imaginary number, and n is the CPE exponent. The value of C can be calculated from eq 6:[58]

$$Q = (CR_{ct})^n/R_{ct} \quad (6)$$

The obtained fitting parameters are presented in Tables 2 and 3. It follows from Table 3 that the Al-5% TiO_2 NP catalyst recorded the lowest charge-transfer resistance value (56.4 Ω cm^2) among the tested catalysts (274.3, 80, and 129.6 Ω cm^2 for Al-1% TiO_2, Al-3% TiO_2, and Al-10% TiO_2 NPs, respectively). This R_{ct} value, namely, 56.4 Ω cm^2, is not too far from that of the commercial Pt/C catalyst (9.1 Ω cm^2; Table 2) but extremely far from that of bare Al (848.7 Ω cm^2; Table 3). These results confirm the polarization measurements (Figure 8 and Table 1) that the nanocomposite of chemical composition Al-5% TiO_2 NPs is the best electrocatalyst for the HER among the studied ones. The largest capacitance value was measured for the Al-5% TiO_2 NP catalyst, demonstrating its large active surface area, as evidenced from Brunauer−Emmett−Teller (BET) measurements. This increased active surface area of a Al-5% TiO_2 NP catalyst promotes its performance for the efficient electrochemical generation of H_2 vide infra.

3.4. Origin of the Catalytic Activity. *3.4.1. TiO_2 NPs as Active Catalytic Sites for the HER.* The presence of TiO_2 NP particles in the Al matrix are the main reason behind the enhanced HER activity of the tested materials. Their nanoeffect (small size and high dispersion) provides the catalyst surface with active adsorption sites for the HER. It can be proposed here that each TiO_2 NP acts as a localized cathode in the Al matrix during the process of cathodic evolution of hydrogen. This, in turn, causes rapid H_2 generation because of the galvanic corrosion effect between the TiO_2 NPs and Al matrix.

3.4.2. Catalysis due to Increased Specific Surface Area (BET Measurements). The large electrochemical surface area of such catalysts induced by the nanoeffect of TiO_2 NPs included in the matrix may be another reason for their increased HER catalytic activity. The small size, high density (number of TiO_2 NPs per unit surface area of the Al matrix), and high dispersion (and, hence, uniform distribution of TiO_2 NPs within the matrix) of such NPs are important parameters for increasing the active (real) surface area of the tested catalysts. BET measurements (Supporting Information, Table S3) showed that the specific surface area (S) of the bare sintered Al is increased from 17 cm^2 mg^{-1} to 29, 47, 97, and 37 cm^2 g^{-1} for Al-1% TiO_2 NP, Al-3% TiO_2 NP, Al-5% TiO_2 NP, and Al-10% TiO_2 NP catalysts, respectively. This adds other evidence for the superior HER electrocatalytic activity of our synthesized Al-TiO_2 nanocomposites compared with bare Al. On the basis of BET measurements, which showed a systematic increase in S with an increase in the content of TiO_2 NPs from 1% up to 5%, the HER catalytic activity of such catalysts is expected to be enhanced following the sequence Al < Al-1% TiO_2 NPs < Al-3% TiO_2 NPs < Al-5% TiO_2 NPs. The results of the electrochemical measurements (Figures 8 and 9, curves 7−10) showed the same sequence of increased HER activity of such catalysts. Therefore, these findings present increased specific surface area of these materials as an important controlling parameter for their enhanced HER activity. This increase in the active area is expected to favor the exposure of more active sites (i.e., TiO_2 NPs) for the HER, thus generating H_2 at lower ovepotentials with high cathodic currents.

A further increase in the amount of TiO_2 NPs (10%) added to the matrix has resulted in an obvious decrease in the value of S (37 cm^2 g^{-1}) and a subsequent decrease in the HER catalytic activity. In this work, the lower HER activity of the catalyst Al-10% TiO_2 NPs (curve 10) compared with those of catalysts Al-3% TiO_2 NPs (curve 8) and Al-5% TiO_2 NPs (curve 9) was a highly reproducible phenomenon. The high content of the TiO_2 NPs included in the matrix of the Al-10% TiO_2 nanocomposite catalyst can be considered as the main reason behind the low HER activity of that catalyst. This high

DOI: 10.1021/acsami.6b05630
ACS Appl. Mater. Interfaces XXXX, XXX, XXX−XXX

Table 3. Mean Value (Standard Deviation) of the Various Electrochemical Parameters Obtained from Impedance Measurements for the HER on the Surfaces of Our Synthesized Al-x% TiO_2 (x = 1, 3, 5, and 10) Nanocomposites[a]

tested cathode	R_s (Ω cm^2)	Q_1 [$s^n(\omega^{-1}$cm$^{-2})$]	R_1(Ω cm^2)	n_1	C_1 (μF cm^{-2})	R_L (Ω cm^2)	L (H cm^2)	Q_2 [$s^n(\omega^{-1}$cm$^{-2})$]	R_2 (Ω cm^2)	R_{ct} (Ω cm^2)	n_2	C_2 (μF cm^{-2})
bare Al	2.23(0.05)	39.02(0.52)	504.7(4.78)	0.88	22.84(0.24)	64.1(1.3)	58.6(0.74)	22.7(0.46)	344(3.8)	848.7(8.58)	0.91	14.05(0.32)
Al-1% TiO_2	2.4(0.07)	104.73(2.2)	175.5(1.82)	0.89	63.91(0.98)	28.5(0.58)	42.8(0.6)	58.9(0.66)	98.8(1.4)	274.3(3.22)	0.9	33.22(0.58)
Al-3% TiO_2	2.33(0.05)	228.89(2.6)	63.4(1.02)	0.91	150.6(1.77)	3.2(0.07)	23.8(0.44)	164.9(1.8)	16.6(0.44)	80(1.46)	0.92	98.7(1.2)
Al-5% TiO_2	2.15(0.06)	683.41(6.2)	31.6(0.66)	0.92	489.6(5.04)	3.8(0.05)	22.05(0.32)	410.7(4.7)	24.8(0.31)	56.4(0.97)	0.91	260.92(3.3)
Al-10% TiO_2	2.27(0.07)	154.02(1.9)	98.4(1.93)	0.9	96.7(1.17)	5.6(0.11)	26.7(38)	117.7(1.6)	31.2(0.52)	129.6(2.45)	0.89	58.83(0.92)

[a]Measurements were performed in 0.5 M H_2SO_4 solutions at a cathodic potential of −0.5 V (SCE) at 25 °C.

population of TiO_2 NPs permits NP aggregation. As a result, the inhomogeneous distribution of TiO_2 NPs in the matrix results revisit Figure 5. Aggregations of TiO_2 NPs and their inhomogeneous distribution in the matrix may account for the lower S value recorded for the Al-10% TiO_2 NP catalyst compared with Al-(1−5%) TiO_2 NP catalysts, with their TiO_2 NPs almost uniformly distributed in their matrices. The high S value (97 cm^2 g^{-1}) of our best catalyst, the Al-5% TiO_2 NP, due to the higher number and homogeneous distribution of TiO_2 NPs, may be one of the main reasons behind its outstanding performance toward the HER compared with the rest of the tested catalysts.

3.5. Long-Term Stability. As shown above, the nanocomposite material of chemical composition Al-5% TiO_2 NPs recorded the highest electrocatalytic performance for the HER among the studied nanocomposites, the reason why it was designated here as the best electrocatalyst. However, a promising electrocatalyst should exhibit good durability (stability) besides its high activity. The long-term stability of the best catalyst was tested by repetitive cycling to form 10000 cycles because intense stability tests in excess of 10000 potential cycles are recommended for real working devices.[59] Figure 11 shows the activity of the Al-5% TiO_2 NP catalyst before and after application of 10000 cycles in a 0.5 M H_2SO_4 solution at a scan rate of 50 mV s^{-1} at 25 °C. Negligible loss of the cathodic current density was observed after the 10000th cycle.

These findings reveal that the nanocomposite of chemical composition Al-5% TiO_2 NPs is highly durable and stable during the electrochemical generation of H_2. Its stability is comparable with that of other recently reported nanocomposite electrocatalysts.[60,61] The excellent durability of that catalyst may originate from the superior electrochemical stability and corrosion resistance of the additives (TiO_2 NPs) and spontaneous passivation of Al, as evidenced from XPS (Figure 6). Chronoamperometry measurements, inset of Figure 11, revealed more information about the electrocatalytic activity and stability of the tested catalysts. The results show an initial linear decrease in the cathodic current from ∼0.25 A cm^{-2}, reaching its minimum value at ∼0.08 A cm^{-2} within the first 25 min of the run. The current then declines, denoting catalyst activation due to H_2 release, to a reasonably steady value at ∼0.15 A cm^{-2} over the 24 h of continuous operation. The initial decrease in the cathodic current refers to catalyst deactivation, most probably due to catalyst poisoning and/or H_2 bubble accumulation.[62] This current−time profile was highly reproducible in this work (Supporting Information, Figure S10).

4. CONCLUSION

In this work, the Al-TiO_2 nanocomposites of various amounts (1, 3, 5, and 10 wt %) of TiO_2 NPs were prepared by a powder metallurgy route via mixing an Al powder (purity 99.7%; size 35 μm) with various amounts of hydrothermally synthesized hydrogen TNTs. The mixture is subjected to compaction under an applied uniaxial stress of 300 MPa, followed by sintering at 500 °C for 1 h. Sintering has converted TNTs into TiO_2 NPs of an average size of 15 nm. The as-prepared Al-TiO_2 nanocomposites were tested as electrocatalysts for the HER in deaerated 0.5 M H_2SO_4 solutions employing polarization and impedance measurements. Results showed that the HER went faster when sintered Al and TiO_2 NPs are brought together as composite materials than if they work individually, demonstrat-

DOI: 10.1021/acsami.6b05630
ACS Appl. Mater. Interfaces XXXX, XXX, XXX−XXX

Table 4. Mean Value (Standard Deviation) of the Amount of H_2 Produced per Hour by Electrolysis[a], Together with the Faradaic Efficiency Values, ε (%), for Our Synthesized Al-x% TiO_2 (x = 1, 3, 5, and 10) Nanocomposite Catalysts, in a Comparison with Those Recorded for Pt/C

		H_2 calculated based on the charge passed during electrolysis		
catalyst	H_2 measured by gas chromatography during electrolysis (H_2 μmol h^{-1})	charge passed (C)	H_2 μmol h^{-1}	ε (%)
Al-1% TiO_2 NPs	6.24(0.12)	1.54(0.04)	7.98(0.17)	78.2(0.13)
Al-3% TiO_2 NPs	8.82(0.15)	1.98(0.05)	10.26(0.21)	85.96(0.24)
Al-5% TiO_2 NPs (the best catalyst)	11.87(0.22)	2.466(0.07)	12.78(0.3)	92.88(0.38)
Al-10% TiO_2 NPs	7.28(0.15)	1.72(0.055)	8.91(0.23)	81.7(0.35)
Pt/C	15.28(0.10)	2.95(0.026)	15.3(0.11)	99.9(0.05)

[a]Electrolysis was carried out by holding the electrode at −0.7 V vs RHE for 1 h in a 0.5 M H_2SO_4 solution.

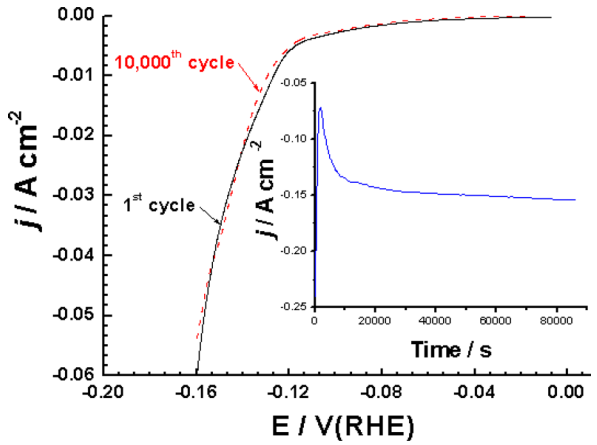

Figure 11. Material stability: effect of repetitive cycling (10000 cycles; scan rate 50 mV s^{-1}) on the electrocatalytic hydrogen evolution of Al-5% TiO_2 NPs (the best catalyst). Inset: Chronoamperometry measurements (j vs t) recorded on the best catalyst at a constant applied potential of −0.2 V vs RHE. All of the stability tests were carried out in 0.5 M H_2SO_4 solutions at 25 °C.

ing cooperative interactions (synergistic effects) between Al and TiO_2 NPs. The high HER activity of these materials was attributed mainly to the abundance of active catalytic sites (i.e., TiO_2 NPs) and the increased electrochemically accessible surface area. The HER activity of such nanocomposites is found to increase with the amount of TiO_2 NPs, reaching its maximum value when the TiO_2 NP content is 5 wt %, and then drops afterward (with 10 wt % TiO_2). The negative influence of the high content of TiO_2 NPs (10 wt %) on the HER activity of the nanocomposites was attributed to the inhomogeneous distribution of TiO_2 NPs in the Al matrix as a result of TiO_2 NP aggregations. The best catalyst, namely, Al-5% TiO_2 NPs, exhibited a high HER activity with a Tafel slope and an exchange current density of 59.8 mV dec^{-1} and 0.14 mA cm^{-2}, which are not far from those of the commercial Pt/C catalyst (31 mV dec^{-1} and 0.78 mA cm^{-2}). The best catalyst also showed good stability after 10000 repetitive cycles with a negligible loss in current.

■ ASSOCIATED CONTENT

Supporting Information

The Supporting Information is available free of charge on the ACS Publications website at DOI: 10.1021/acsami.6b05630.

DSC, DTA, and TGA curves for hydrogen TNTs, conversion of the working electrode's potential from the SCE to RHE scale, data from XRD and XPS examinations, SEM/EDX examinations of the tested composites, XPS depth profile of Al-TiO_2 NPs, determination of the exchange current density, calculation of the TOF values for each tested material, tabular comparison of the HER activity of Al-5% TiO_2 NPs with the reported literature, H_2 generation calculated from gas chromatography, charge versus time plots recorded for Al-TiO_2 NP catalysts and comparison, Bode plots for the tested materials, complex-plane impedance plots for the tested materials, equivalent circuits used to fit the EIS data, and chronoamperometry measurements of the best catalyst (PDF)

■ AUTHOR INFORMATION

Corresponding Author

*E-mail: maaismail@yahoo.com. Tel: +966560480239. Fax: +966(0)127329494.

Notes

The authors declare no competing financial interest.

■ ACKNOWLEDGMENTS

This work was supported by Taif University (Kingdom of Saudi Arabia) through Project 1-145-3716. The authors are also grateful to the Director, CSIR−NEIST, Jorhat, India, for his interest in carrying out the work. G.D. acknowledges DST, New Delhi, India, for a DST-INSPIRE Fellowship grant.

■ REFERENCES

(1) Armand, M.; Tarascon, J.-M. Building Better Batteries. *Nature* **2008**, *451*, 652−657.
(2) Bockris, J. O. M. The Origin of Ideas on a Hydrogen Economy and its Solution to the Decay of the Environment. *Int. J. Hydrogen Energy* **2002**, *27*, 731−740.
(3) Morales-Guio, C. G.; Stern, L.-A.; Hu, X. Nanostructured Hydrotreating Catalysts for Electrochemical Hydrogen Evolution. *Chem. Soc. Rev.* **2014**, *43*, 6555−6569.
(4) Mason, J. E. World energy analysis: H_2 now or later? *Energy Policy* **2007**, *35*, 1315−1329.
(5) Cheng, W. H.; Shiau, C. Y.; Liu, T. H.; Tung, H. L.; Lu, J. F.; Hsu, C. C. Promotion of Cu/Cr/Mn Catalyst by Alkali Additives in Methanol Decomposition. *Appl. Catal., A* **1998**, *170*, 215−224.
(6) Zou, X.; Zhang, Y. Noble Metal-free Hydrogen Evolution Catalysts for Water Splitting. *Chem. Soc. Rev.* **2015**, *44*, 5148−5180.
(7) Brown, L. F. A Comparative Study of Fuels for on-board Hydrogen Production for Fuel-cell-Powered Automobiles. *Int. J. Hydrogen Energy* **2001**, *26*, 381−397.
(8) Belitskus, D. Electrolytic Removal of P-Type GaAs Substrates from Thin, N-Type Semiconductor Layers. *J. Electrochem. Soc.* **1970**, *117*, 1097.

DOI: 10.1021/acsami.6b05630
ACS Appl. Mater. Interfaces XXXX, XXX, XXX−XXX

(9) Zeng, M.; Li, Y. Recent Advances in Heterogeneous Electrocatalysts for the Hydrogen Evolution Reaction. *J. Mater. Chem. A* **2015**, *3*, 14942−14962.
(10) Jiao, F.; Frei, H. Nanostructured Cobalt and Manganese Oxide Clusters as Efficient Water Oxidation Catalysts. *Energy Environ. Sci.* **2010**, *3*, 1018−1027.
(11) Merki, D.; Hu, X. L. Recent Developments of Molybdenum and Tungsten Sulfides as Hydrogen Evolution Catalysts. *Energy Environ. Sci.* **2011**, *4*, 3878−3888.
(12) Laursen, A. B.; Kegnaes, S.; Dahl, S.; Chorkendorff, I. Molybdenum sulfides - Efficient and Viable Materials for Electro- and Photoelectrocatalytic Hydrogen Evolution. *Energy Environ. Sci.* **2012**, *5*, 5577−5591.
(13) Amin, M. A.; Fadlallah, S. A.; Alosaimi, G. S. In Situ Aqueous Synthesis of Silver Nanoparticles Supported on Titanium as Active Electrocatalyst for the Hydrogen Evolution Reaction. *Int. J. Hydrogen Energy* **2014**, *39*, 19519−19540.
(14) Amin, M. A.; Fadlallah, S. A.; Alosaimi, G. S.; Kandemirli, F.; Saracoglu, M.; Szunerits, S.; Boukherroub, R. Cathodic Activation of Titanium-Supported Gold Nanoparticles: An Efficient and Stable Electrocatalyst for the Hydrogen Evolution Reaction. *Int. J. Hydrogen Energy* **2016**, *41*, 6326−6341.
(15) Darabdhara, G.; Amin, M. A.; Mersal, G. A. M.; Ahmed, E. M.; Das, M. R.; Zakaria, M. B.; Malgras, V.; Alshehri, S. M.; Yamauchi, Y.; Szunerits, S.; Boukherroub, R. Reduced Graphene Oxide Nanosheets Decorated with Au, Pd and Au-Pd Bimetallic Nanoparticles as Highly Efficient Catalysts for Electrochemical Hydrogen Generation. *J. Mater. Chem. A* **2015**, *3*, 20254−20266.
(16) Raj, I. A.; Vasu, K. I. Transition Metal-Based Hydrogen Electrodes in Alkaline Solution - Electrocatalysis on Nickel Based Binary Alloy Coatings. *J. Appl. Electrochem.* **1990**, *20*, 32−38.
(17) Deng, J.; Ren, P.; Deng, D.; Bao, X. Enhanced Electron Penetration through an Ultrathin Graphene Layer for Highly Efficient Catalysis of the Hydrogen Evolution Reaction. *Angew. Chem., Int. Ed.* **2015**, *54*, 2100−2104.
(18) Li, J.; Zhou, P.; Li, F.; Ren, R.; Liu, Y.; Niu, J.; Ma, J.; Zhang, X.; Tian, M.; Jin, J.; Ma, J. Ni@Pd/PEI-rGO Stack Structures with Controllable Pd Shell Thickness as Advanced Electrodes for Efficient Hydrogen Evolution. *J. Mater. Chem. A* **2015**, *3*, 11261−11268.
(19) Lv, H.; Xi, Z.; Chen, Z.; Guo, S.; Yu, Y.; Zhu, W.; Li, Q.; Zhang, X.; Pan, M.; Lu, G.; Mu, S.; Sun, S. A New Core/Shell NiAu/Au Nanoparticle Catalyst with Pt-like Activity for Hydrogen Evolution Reaction. *J. Am. Chem. Soc.* **2015**, *137*, 5859−5862.
(20) Guo, X.; Cao, G.-l.; Ding, F.; Li, X.; Zhen, S.; Xue, Y.-F.; Yan, Y.-M.; Liu, T.; Sun, K.-N. A Bulky and Flexible Electrocatalyst for Efficient Hydrogen Evolution Based on the Growth of MoS_2 Nanoparticles on Carbon Nanofiber Foam. *J. Mater. Chem. A* **2015**, *3*, 5041−5046.
(21) Cheng, L.; Huang, W. J.; Gong, Q. F.; Liu, C. H.; Liu, Z.; Li, Y. G.; Dai, H. J. Ultrathin WS_2 Nanoflakes as a High-Performance Electrocatalyst for the Hydrogen Evolution Reaction. *Angew. Chem., Int. Ed.* **2014**, *53*, 7860−7863.
(22) Garcia-Esparza, A. T.; Cha, D.; Ou, Y. W.; Kubota, J.; Domen, K.; Takanabe, K. Tungsten Carbide Nanoparticles as Efficient Cocatalysts for Photocatalytic Overall Water Splitting. *ChemSusChem* **2013**, *6*, 168−181.
(23) Pan, L. F.; Li, Y. H.; Yang, S.; Liu, P. F.; Yu, M. Q.; Yang, H. G. Molybdenum Carbide Stabilized on Graphene with High Electrocatalytic Activity for Hydrogen Evolution Reaction. *Chem. Commun.* **2014**, *50*, 13135−13137.
(24) Xie, J.; Li, S.; Zhang, X.; Zhang, J.; Wang, R.; Zhang, H.; Pan, B.; Xie, Y. Atomically-Thin Molybdenum Nitride Nanosheets with Exposed Active Surface Sites for Efficient Hydrogen Evolution. *Chem. Sci.* **2014**, *5*, 4615−4620.
(25) Vrubel, H.; Hu, X. L. Molybdenum Boride and Carbide Catalyze Hydrogen Evolution in both Acidic and Basic Solutions. *Angew. Chem., Int. Ed.* **2012**, *51*, 12703−12706.
(26) Popczun, E. J.; Read, C. G.; Roske, C. W.; Lewis, N. S.; Schaak, R. E. Highly Active Electrocatalysis of the Hydrogen Evolution Reaction by Cobalt Phosphide Nanoparticles. *Angew. Chem., Int. Ed.* **2014**, *53*, 5427−5430.
(27) Yu, J.; Qi, L.; Jaroniec, M. Hydrogen Production by Photocatalytic Water Splitting over Pt/TiO_2 Nanosheets with Exposed (001) Facets. *J. Phys. Chem. C* **2010**, *114*, 13118−13125.
(28) Wang, X.; Yu, J. C.; Ho, C.; Hou, Y.; Fu, X. Photocatalytic Activity of a Hierarchically Macro/Mesoporous Titania. *Langmuir* **2005**, *21*, 2552−2559.
(29) Unosson, E.; Welch, K.; Persson, C.; Engqvist, H. Stability and Prospect of UV/H_2O_2 Activated Titania Films for Biomedical Use. *Appl. Surf. Sci.* **2013**, *285*, 317−323.
(30) Litter, M. I.; Navio, J. A. Photocatalytic Properties of Iron-Doped Titania Semiconductors. *J. Photochem. Photobiol., A* **1996**, *98*, 171−181.
(31) Mohapatra, S. K.; Misra, M.; Mahajan, V. K.; Raja, K. S. Design of a Highly Efficient Photoelectrolytic Cell for Hydrogen Generation by Water Splitting: Application of TiO_2-xCx Nanotubes as a Photoanode and Pt/TiO_2 Nanotubes as a Cathode. *J. Phys. Chem. C* **2007**, *111*, 8677−8685.
(32) Lai, Y.; Gong, J.; Lin, C. Self-organized TiO_2 Nanotube Arrays with Uniform Platinum Nanoparticles for Highly Efficient Water Splitting. *Int. J. Hydrogen Energy* **2012**, *37*, 6438−6446.
(33) Subramanian, V.; Wolf, E.; Kamat, P. Semiconductor-Metal Composite Nanostructures. To What Extent Do Metal Nanoparticles Improve the Photocatalytic Activity of TiO_2 Films? *J. Phys. Chem. B* **2001**, *105*, 11439−11446.
(34) Lee, C. K.; Liu, S. S.; Chen, H. C. Application of Hydrothermal Method Derived Titanate Nanotubes as Adsorbents. Recent Pat. *Recent Pat. Nanotechnol.* **2009**, *3*, 203−212.
(35) Zhang, Q.; Li, Y.; Ackerman, E. A.; Gajdardziska-Josifovska, M.; Li, H. Visible Light Responsive Iodine-Doped TiO_2 for Photocatalytic Reduction of CO_2 to Fuels. *Appl. Catal., A* **2011**, *400*, 195−202.
(36) Siuzdak, K.; Szkoda, M.; Lisowska-Oleksiak, A.; Grochowska, K.; Karczewski, J.; Ryl, J. Thin Layer of Ordered Boron-Doped TiO_2 Nanotubes Fabricated in a Novel Type of Electrolyte and Characterized by Remarkably Improved Photoactivity. *Appl. Surf. Sci.* **2015**, *357*, 942−950.
(37) Abreu, C. M.; Cristobal, M. J.; Figuroa, R.; Pena, G. Passive Layers Developed on Different Tempers of AA7075 Aluminium Alloy After Molybdenum Implantation. *Surf. Interface Anal.* **2012**, *44*, 1039−1044.
(38) Kobotiatis, L.; Pebere, N.; Koutsoukos, P. G. Study of the Electrochemical Behavior of the 7075 Aluminum Alloy in the Presence of Sodium Oxalate. *Corros. Sci.* **1999**, *41*, 941−957.
(39) Ryl, J.; Wysocka, J.; Jarzynka, M.; Zielinski, A.; Orlikowski, J.; Darowicki, K. Effect of Native Air-Formed Oxidation on the Corrosion Behavior of AA 7075 Aluminum Alloys. *Corros. Sci.* **2014**, *87*, 150−155.
(40) Diplas, S.; Watts, J. F.; Tsakiropoulos, P.; Shao, G.; Beamson, G.; Matthew, J. A. D. X-ray Photoelectron Spectroscopy Studies of Ti-Al and Ti-Al-V Alloys Using Cr Kβ Radiation. *Surf. Interface Anal.* **2001**, *31*, 734−744.
(41) Tang, H.; Dou, K. P.; Kaun, C. C.; Kuang, Q.; Yang, S. H. $MoSe_2$ Nanosheets and their Graphene Hybrids: Synthesis, Characterization and Hydrogen Evolution Reaction Studies. *J. Mater. Chem. A* **2014**, *2*, 360−364.
(42) Wang, T.; Liu, L.; Zhu, Z.; Papakonstantinou, P.; Hu, J.; Liu, H.; Li, M. Enhanced Electrocatalytic Activity for Hydrogen Evolution Reaction From Self-Assembled Monodispersed Molybdenum Sulfide Nanoparticles on an Au Electrode. *Energy Environ. Sci.* **2013**, *6*, 625−633.
(43) Bard, A. J.; Faulkner, L. R. *Electrochemical Methods: Fundamental and Applications*, 2nd ed.; John Wiley and Sons, Inc.: New York, 2001.
(44) Xia, M.; Lei, T.; Lv, N.; Li, N. Synthesis and Electrocatalytic Hydrogen Evolution Performance of Ni-Mo-Cu Alloy Coating Electrode. *Int. J. Hydrogen Energy* **2014**, *39*, 4794−4802.
(45) Solmaz, R.; Kardas, G. Fabrication and Characterization of NiCoZn−M (M: Ag, Pd and Pt) Electrocatalysts as Cathode Materials

DOI: 10.1021/acsami.6b05630
ACS Appl. Mater. Interfaces XXXX, XXX, XXX−XXX

for Electrochemical Hydrogen Production. *Int. J. Hydrogen Energy* **2011**, *36*, 12079−12087.
(46) Rodriguez-Valdez, L.; Guel, I. E.; Calderón, F. A.; Neri-Flores, M. A.; Villafane, A. M.; Sánchez, R. M. Electrochemical Performance of Hydrogen Evolution Reaction of Ni-Mo Electrodes Obtained by Mechanical Alloying. *Int. J. Hydrogen Energy* **2004**, *29*, 1141−1145.
(47) Sun, Y.; Liu, C.; Grauer, D. C.; Yano, J.; Long, J. R.; Yang, P.; Chang, C. J. Electrodeposited Cobalt-Sulfide Catalyst for Electrochemical and Photoelectrochemical Hydrogen Generation from Water. *J. Am. Chem. Soc.* **2013**, *135*, 17699−17702.
(48) Tran, P. D.; Nguyen, M.; Pramana, S. S.; Bhattacharjee, A.; Chiam, S. Y.; Fize, J.; Field, M. J.; Artero, V.; Wong, L. H.; Loo, J.; Barber, J. L. Copper Molybdenum Sulfide: A New Efficient Electrocatalyst for Hydrogen Production from Water. *Energy Environ. Sci.* **2012**, *5*, 8912−8916.
(49) Huang, X.; Zeng, Z. Y.; Bao, S. Y.; Wang, M. F.; Qi, X. Y.; Fan, Z. X.; Zhang, H. Solution-Phase Epitaxial Growth of Noble Metal Nanostructures on Dispersible Single-Layer Molybdenum Disulfide-nanosheets. *Nat. Commun.* **2013**, *4*, 1444.
(50) Kibsgaard, J.; Jaramillo, T. F. Molybdenum Phosphosulfide: An Active, Acid-Stable, Earth-Abundant Catalyst for the Hydrogen Evolution Reaction. *Angew. Chem., Int. Ed.* **2014**, *53*, 14433−14437.
(51) Kibsgaard, J.; Chen, Z.; Reinecke, B. N.; Jaramillo, T. F. Engineering the Surface Structure of MoS_2 to Preferentially Expose Active Edge Sites for Electrocatalysis. *Nat. Mater.* **2012**, *11*, 963−969.
(52) Danaee, I.; Noori, S. Kinetics of the Hydrogen Evolution Reaction on NiMn Graphite Modified Electrode. *Int. J. Hydrogen Energy* **2011**, *36*, 12102−12111.
(53) Rehim, S. S. A.; Hassan, H. H.; Amin, M. A. Corrosion and Corrosion Inhibition of Al and Some Alloys in Sulphate Solutions Containing Halide Ions Investigated by an Impedance Technique. *Appl. Surf. Sci.* **2002**, *187*, 279−290.
(54) Khaled, K. F.; Amin, M. A. Electrochemical and Molecular Dynamics Simulation Studies on the Corrosion Inhibition of Aluminum in Molar Hydrochloric Acid Using Some Imidazole Derivatives. *J. Appl. Electrochem.* **2009**, *39*, 2553−2568.
(55) Lenderink, H. J. W.; Linden, M. V. D.; De Wit, J. H. W. Corrosion of Aluminum in Acidic and Neutral Solutions. *Electrochim. Acta* **1993**, *38*, 1989−1992.
(56) Ryl, J.; Darowicki, K. Impedance Monitoring of Carbon Steel Cavitation Erosion under the Influence of Corrosive Factors. *J. Electrochem. Soc.* **2008**, *155*, 44−49.
(57) McCafferty, E. On the Determination of Distributed Double-Layer Capacitances from Cole-Cole plots. *Corros. Sci.* **1997**, *39*, 243−254.
(58) Wu, X.; Ma, H.; Chen, S.; Xu, Z.; Sui, S. General Equivalent Circuits for Faradaic Electrode Processes under Electrochemical Reaction Control. *J. Electrochem. Soc.* **1999**, *146*, 1847−1853.
(59) Benson, J.; Li, M.; Wang, S.; Papakonstantinou, P.; Wang, P. Electrocatalytic Hydrogen Evolution Reaction on Edges of a Few Layer Molybdenum Disulfide Nanodots. *ACS Appl. Mater. Interfaces* **2015**, *7*, 14113−14122.
(60) Roy, N.; Leung, K. T.; Pradhan, D. Nitrogen Doped Reduced Graphene Oxide Based Pt-TiO_2 Nanocomposites for Enhanced Hydrogen Evolution. *J. Phys. Chem. C* **2015**, *119*, 19117−19125.
(61) Lai, F.; Miao, Y.-E.; Huang, Y.; Zhang, Y.; Liu, T. Nitrogen-Doped Carbon Nanofiber/Molybdenum Disulfide Nanocomposites Derived from Bacterial Cellulose for High-Efficiency Electrocatalytic Hydrogen Evolution Reaction. *ACS Appl. Mater. Interfaces* **2016**, *8*, 3558−3566.
(62) Xie, J. F.; Zhang, H.; Li, S.; Wang, R. X.; Sun, X.; Zhou, M.; Zhou, J. F.; Lou, X. W.; Xie, Y. Defect-Rich MoS_2 Ultrathin Nanosheets with Additional Active Edge Sites for Enhanced Electrocatalytic Hydrogen Evolution. *Adv. Mater.* **2013**, *25*, 5807−5813.

DOI: 10.1021/acsami.6b05630
ACS Appl. Mater. Interfaces XXXX, XXX, XXX−XXX